

MXene-Nanoflakes-Enabled All-Optical Nonlinear Activation Function for On-Chip Photonic Deep Neural Networks

Adir Hazan, Barak Ratzker, Danzhen Zhang, Aviad Katiyi, Maxim Sokol, Yury Gogotsi, and Alina Karabchevsky*

2D metal carbides and nitrides (MXene) are promising material platforms for on-chip neural networks owing to their nonlinear saturable absorption effect. The localized surface plasmon resonances in metallic MXene nanoflakes may play an important role in enhancing the electromagnetic absorption; however, their contribution is not determined due to the lack of a precise understanding of its localized surface plasmon behavior. Here, a saturable absorber made of MXene thin film and a silicon waveguide with MXene flakes overlayer are developed to perform neuromorphic tasks. The proposed configurations are reconfigurable and can therefore be adjusted for various applications without the need to modify the physical structure of the proposed MXene-based activator configurations via tuning the wavelength of operation. The capability and feasibility of the obtained results of machine-learning applications are confirmed via handwritten digit classification task, with near 99% accuracy. These findings can guide the design of advanced ultrathin saturable absorption materials on a chip for a broad range of applications.

response prediction of subwavelength nanophotonic devices,^[1] neuromorphic computing,^[2] obtaining the inverse design for a given optical response,^[3–6] single-pixel cameras that capture coded projections of a scene with a single photodetector and computationally recover them,^[7] and others. The utilization of integrated photonics in NNs^[8] offers a promising alternative approach to microelectronic and hybrid optical–electronic implementations, owing to the improvement in computational speed and power efficiency in machine-learning tasks. While implementing NNs optically, the main challenge is in implementing the activation function with nonlinear materials—this is currently still being fulfilled electronically^[9–14] and is time- and power consuming.

A variety of free-space and on-chip activators out of different material platforms and

configurations were reported: microfiber with MXene overlayer,^[15] wavelength specific ring-resonator-based and liquid-crystal-based activator.^[16–18] The activation function made of Mach–Zehnder interferometer integrated on a chip with a ring resonator which requires electrical control, was reported in ref. [19]. Although implemented on a chip, such configuration is sensitive to wavelength deviations. The neuromorphic electrooptic activation function operating optomechanically in free space was reported in refs. [20,21] which eventually converts the optical signal to electronic. Such an activation function is not fully optically operated. In addition, the operation speed of such a device is about five orders of magnitude lower compared to the all-optical activation function (see Figure S7 in the Supporting Information).

To address this challenge, here we utilize the nonlinear properties of MXene ($\text{Ti}_3\text{C}_2\text{T}_x$) and integrated photonics platform to demonstrate a novel concept of the NN activation function implemented all-optically^[22–24] on a chip, specifically the effect related to the imaginary part of the $\chi^{(3)}$ optical nonlinearity and field localization effects in MXene nanoflake overlayer on silicon rib waveguide (WG). Integrated photonics provides a stable, compact, and robust platform to implement complex photonic circuits,^[25] and therefore is a compelling technology for the realization of photonic NN with a time delay on the order of picoseconds.

Unlike conventional nonlinear activation function mechanisms, which are based on devices that convert an optical signal into an electrical signal, then by applying the nonlinearity to convert it back into an optical signal—resulting in slower computational speed and noise—we utilize the optical effects of novel 2D material MXene. MXenes comprise a large class of 2D

1. Introduction

Artificial neural networks (NNs) are computational network models which are inspired by the way the signals are processed in the brain. NNs have been implemented in numerous integrated photonics applications. These include the optical

A. Hazan, A. Katiyi, A. Karabchevsky
 School of Electrical and Computer Engineering
 Electro-Optics and Photonics Engineering Department
 Ben-Gurion University of the Negev
 Beer-Sheva 8410501, Israel
 E-mail: alinak@bgu.ac.il

B. Ratzker, M. Sokol
 Department of Materials Science and Engineering
 Tel Aviv University
 Ramat Aviv 6997801, Israel

D. Zhang, Y. Gogotsi
 A. J. Drexel Nanomaterials Institute and Department of Materials
 Science and Engineering
 Drexel University
 Philadelphia, PA 19104, USA

The ORCID identification number(s) for the author(s) of this article can be found under <https://doi.org/10.1002/adma.202210216>.

© 2023 The Authors. Advanced Materials published by Wiley-VCH GmbH. This is an open access article under the terms of the Creative Commons Attribution-NonCommercial-NoDerivs License, which permits use and distribution in any medium, provided the original work is properly cited, the use is non-commercial and no modifications or adaptations are made.

DOI: 10.1002/adma.202210216

transition metal carbides and nitrides such as $\text{Ti}_3\text{C}_2\text{T}_x$ (T_x represents surface terminations such as $-\text{O}$, $-\text{OH}$, and $-\text{F}$).^[26,27] They exhibit unique light–matter interactions, such as the nonlinear effect^[28] of saturable absorption^[29] on the one hand, and plasmonic properties on the other hand.^[30,31] Furthermore, integrating MXene in photonic circuits is extremely useful for the all-optical nonlinear activation function in NN. MXene on a chip is affordable and simple to fabricate architecture as compared to the conventional architectures as in ref. [S1] (Supporting Information).

The integration of the nonlinear optical unit in a photonic circuit remains an open challenge, along with strengthening modulation and increasing operational speed, to increase the effectiveness at both the device and system levels. To address this challenge, we propose mechanisms for implementing the NN activation function based on saturable absorption, which does not require electrical or temperature controls. Recently, theoretical work on an all-optical nonlinear activation function based on a saturable absorber was proposed in refs. [22,32] but has never been proved experimentally. Here, we demonstrate the nonlinear activation function on a chip. The concept of an all-optically implemented nonlinear activation function on a chip that we propose is expected to be the most energy-efficient and operate at a fivefold higher processing speed than existing conventional NNs implemented electronically and can therefore compete with conventional von Neumann computer architecture.

Here, we demonstrate the optical neuron nonlinear activation function based on nanophotonic structures. Specifically, we use: 1) a saturable absorber made of $\text{Ti}_3\text{C}_2\text{T}_x$ MXene thin film, and 2) a nanophotonic silicon-on-insulator multimode rib waveguide covered with MXene flakes. We test them experimentally and develop a NN-based emulator to analyze the results. The nonlinear

activation function with executed Modified National Institute of Standards and Technology (MNIST) database handwritten digit classification task reported here is of 99.1% accuracy.

2. Results

2.1. Nanophotonic Neural Network Mechanism of Operation

The concept of the fundamental building block for a fully integrated deep structured learning, as illustrated in **Figure 1a**, represents an entire deep-NN (DNN) layer using a MXene overlayer on a chip to introduce nonlinear properties in the network. The optical signals carrying encoded information that propagates via a linear combination of the inputs arriving from the preceding building block (i.e., a layer) pass through the nonlinear activation function. This function eventually serves as an input to the next building block unit. In general, the photonic building blocks can optically implement arbitrary DNN and are defined as a function $f: \mathbb{R}^n \rightarrow \mathbb{R}^m$, where n and m ($n, m \geq 1$) are the number of neurons in the input and output layers, respectively. As shown schematically in **Figure 1b**, a well-known deep-learning architecture consists of input and output layers, with at least one hidden layer. Generally, a feedforward network contains interconnected neurons that do not form a cycle (neurons connect only to different neurons in successive layers). The operating principle of each neuron in the network can be divided into the following two optical interfaces: 1) the linear operation unit involves weighting and summation, and 2) the nonlinearity unit defines the neuron output by generating a new signal given an input.

An optical interference unit (OIU) can be realized using various integrated photonics architectures to implement matrix

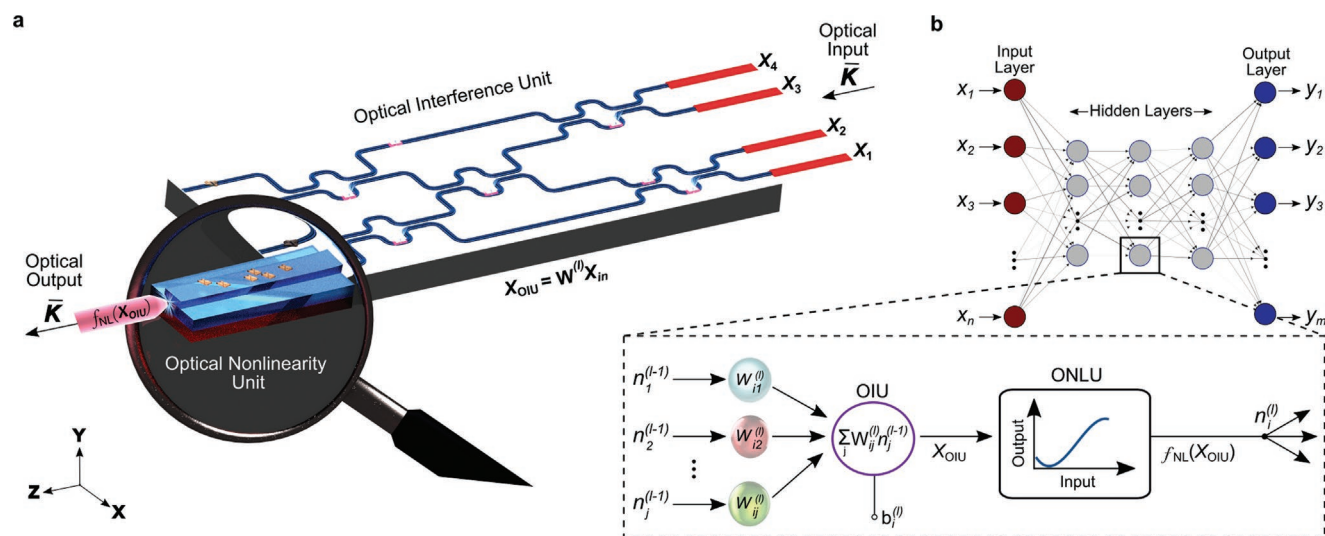


Figure 1. A schematic conceptualization of fully integrated MXene-based DNN building block. a) The rendered chip shows the implementation of a whole layer in DNN via a photonic circuit (gray rectangle). The input laser (red) encodes the information carried through the chip via waveguides (blue). The chip relies on a mesh of Mach–Zehnder interferometers; each consists of directional couplers (curved sections in the waveguides integrated with phase shifters (red glowing objects) to control the splitting ratio and the differential output phase. The zoom-in illustrates the neuron’s nonlinear activation function based on light–MXene interaction, where a rib waveguide is covered with MXene flakes. The arrows indicate the propagation direction of the light. b) General architecture of a fully connected DNN constituted of an input layer (red circles), several hidden layers (gray circles), and an output layer (blue circles); inset shows a schematic of one neuron, the input optical signals are weighted and combined, then the nonlinear activation function is applied.

multiplication for weighting and summation. The physical implementation can be classified as optical mode realization such as linear operation nanophotonics circuits,^[10,33–36] or multiwavelength realization such as parallel weighting of optical carrier signals generated from wavelength-division multiplexing using microring resonator weight banks.^[16,37–40] Those have been demonstrated previously during different computational tasks. For multiple weighted $W_{ij}^{(l)}$ input signals $n_j^{(l-1)}$ arriving from the output of neurons in the previous layer with the addition of a bias $b_i^{(l)}$, the linear optical interface of the i th neuron $n_i^{(l)}$ in the layer l th, is given by a linear operation across all the inputs, i.e., $n_i^{(l)} = b_i^{(l)} + \sum_j W_{ij}^{(l)} n_j^{(l-1)}$. A realistic OIU

building block may be emulated in DNN modeling by considering the analytical form of a whole layer output $X_{\text{OIU}}^{(l)}$, as follows: $X_{\text{OIU}}^{(l)} = W^{(l)} Y^{(l-1)}$, through the forward-propagation procedure. For instance, weighted input signals can be implemented with a nanophotonic circuit of integrated Mach–Zehnder interferometers, each formed of waveguides and 50:50 directional couplers which are combined with phase shifters.^[10,33] In particular, where any unitary transformations can be implemented with conventional optical beam splitters and phase shifters,^[41] a rectangular diagonal matrix can be implemented with optical attenuation achieved by the Mach–Zehnder modulator. As well, an OIU implementation that relies on free-space diffractive DNN^[42–44] has already been shown in the spectral domain.^[45,46] When diffraction light interference implements the weighting, a sum of these signals is achieved through combined transmission (or reflection) coefficients at each point on a given transmissive layer that acts as a neuron. However, an OIU alone is insufficient for a photonic device to act as a building block in DNN applications, and some optical nonlinearities must be introduced. In principle, a photonic neuron generates a new optical output signal processing the multiple optical inputs signals $X_{\text{OIU}}^{(l)}$, through the nonlinear activation function, $n_i^{(l)} = f_{\text{NL}}(X_{\text{OIU}}^{(l)})$. Implementations of optical nonlinearity unit (ONLU) fall into two major categories, one based on optical-to-electrical-to-optical and the other on all-optical (AO). With the help of light–MXene interaction, the nonlinear activation function can be realized in an AO manner.

2.2. Design and Fabrication of MXene-Based All-Optical Nonlinear Activation Function

Generally, an artificial neuron includes multiple weighted input signals followed by nonlinear activation. Focusing on the nonlinear neuron unit, we study its all-optical nonlinear activation functions utilizing unique light–matter interactions in 2D $\text{Ti}_3\text{C}_2\text{T}_x$ —MXene. Here, we validate the photonic DNN performance by focusing on the shape of the activation functions. To this end, the linear operation is emulated with the nonlinear optical activation function, realized with two independent configurations. For this purpose, we engineered two devices to introduce the all-optical nonlinear activation function. **Figure 2a** and the inset of **Figure 5a** show rendered images of studied architectures to demonstrate the concept of an all-optical nonlinear activation function with a MXene overlayer. A nonpolarized electromagnetic wave illuminates the in-facet of a multimode rib waveguide (**Figure 2a**). The interaction with the MXene overlayer takes place via evanescent waves. The unpolarized plane electromagnetic wave illuminates the thin film of MXene on a glass substrate, as shown in the inset of **Figure 5a**. To study the nonlinear response of fabricated samples, two experimental setups operating in a broad spectral range were constructed. For MXene thin films, a coherent supercontinuum generation laser source was focused on the film, and then the light was collected by an optical spectrum analyzer (OSA) via a fiber. For the on-chip configuration, the rib waveguide covered with MXene flakes was butt-coupled via single-mode fiber (connected to a coherent supercontinuum generation laser source), and then the light was collected by OSA via a multimode fiber. In addition, the rib waveguide surfaces were imaged on the camera for inspection, characterization, and alignment.

2.3. Formation of MXene-Flake-Based Metasurface on a Waveguide

One possibility for inducing an optical nonlinearity in a photonic integrated circuit is by exploiting a hybrid system consisting of a silicon waveguide with a MXene flake overlayer.

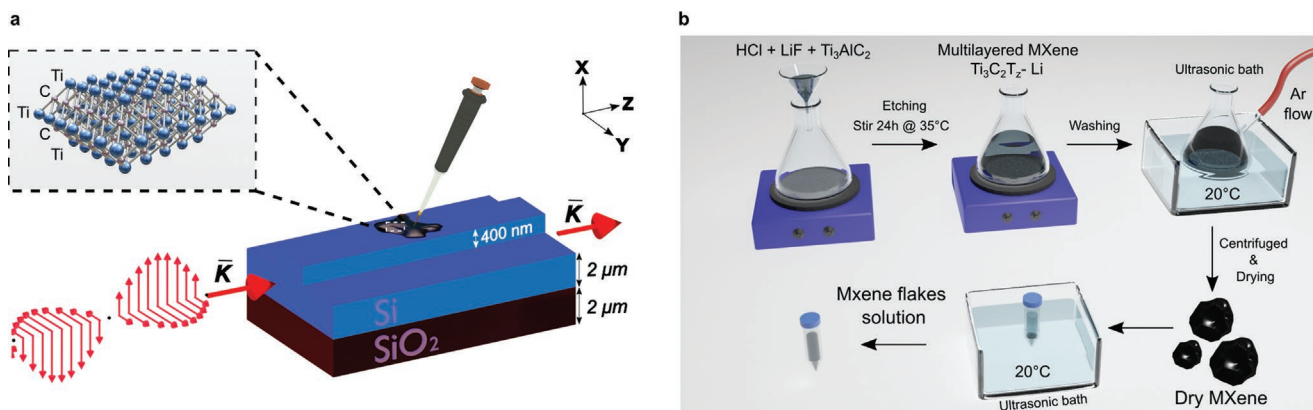


Figure 2. MXene flake production for the rib waveguide overlayer. a) The studied system's artistic design: incident unpolarized light illuminates the rib waveguide facet, which is covered with MXene flakes. The inset shows the crystal structure of a 2D MXene monolayer, $\text{Ti}_3\text{C}_2\text{T}_x$. b) Schematic illustrating the synthesis process of MXene from MAX phases and redispersion of the dry product to produce MXene-dispersed suspension.

Figure 2a shows a rendered image of the studied architecture on a chip to demonstrate the concept of an all-optical nonlinear activation function with a MXene overlayer. Nonpolarized electromagnetic wave illuminates the in-facet of a multimode rib waveguide. The interaction with the MXene overlayer takes place via evanescent waves and: 1) leads to some losses within the material, and 2) causes the scattering of light in all directions. The rib waveguide is wide enough to support multiple modes to increase the coupling between the evanescent waves and MXene nanoflakes. This can be achieved with the higher-order modes that have a longer evanescent field extension into the medium and larger field amplitudes at the waveguide cladding interface, compared to the fundamental and lower modes. To produce a MXene metasurface (a metasurface is a patterned thin film composed of elements at a subwavelength scale to achieve tailored properties), the first $\text{Ti}_3\text{C}_2\text{T}_x$ MXene was synthesized through selective chemical etching using the $\text{LiF} + \text{HCl}$ method.^[47] Then, to realize a MXene-based metasurface, a diluted MXene suspension in water with 0.01 g mL^{-1} was prepared and drop-casted on a waveguide. Figure 2b shows a schematic illustration describing the synthesis process of MXenes from MAX phases and redispersion of the dry product to produce MXene-dispersed suspension.

Concurrently, we fabricated a silicon rib waveguide with a MXene flake overlayer. Figure 3a shows the schematics of an inline experimental setup operating with broadband illumination to test such waveguides. Figure 4a shows transmission spectra

collected via multimode fiber from the distal end of the waveguides with a strip width of $4 \mu\text{m}$ covered by a MXene-flake-based metasurface with well-pronounced spectral signatures: a dip around 1180 nm with a depth of -25 dB and a dip around 1490 nm with a depth of -20 dB . These dips can be associated with plasmonic-excitation-oriented MXene flakes on the waveguide surface. Plasmonic excitation in MXene arises from a plasmon-induced increase in the ground state absorption at photon energies above the threshold for free carrier oscillations.^[29] The dip in transmission spectrum around 1490 nm , shown in Figure 4a, can be associated with the first overtone excitation of $-\text{OH}$ functional group out-of-plane vibrations of MXene.^[48] The first principle calculations^[49] verify the fundamental vibration related to this overtone. The dip in transmission around 1180 nm can be associated with the waveguide-shifted overtone vibration of MXene metasurface assigned to the $\text{OH}/\text{H}_2\text{O}$ native oxide layer on the waveguide surface, or with plasmonic excitation, because the real part of the permittivity of MXene is negative in this range—as can be seen from the dispersion spectra we measured with ellipsometry (shown in Figure S1 in the Supporting Information). In addition, the nanoscale flakes of MXene can exhibit a nanoantenna effect resulting in resonances appearing in transmission spectra. The shallow peak around 980 nm corresponds to the minor peak shown in Figure 4a and can be explained by the MXene dispersion as measured with an ellipsometer (see Figure S1 in the Supporting Information).

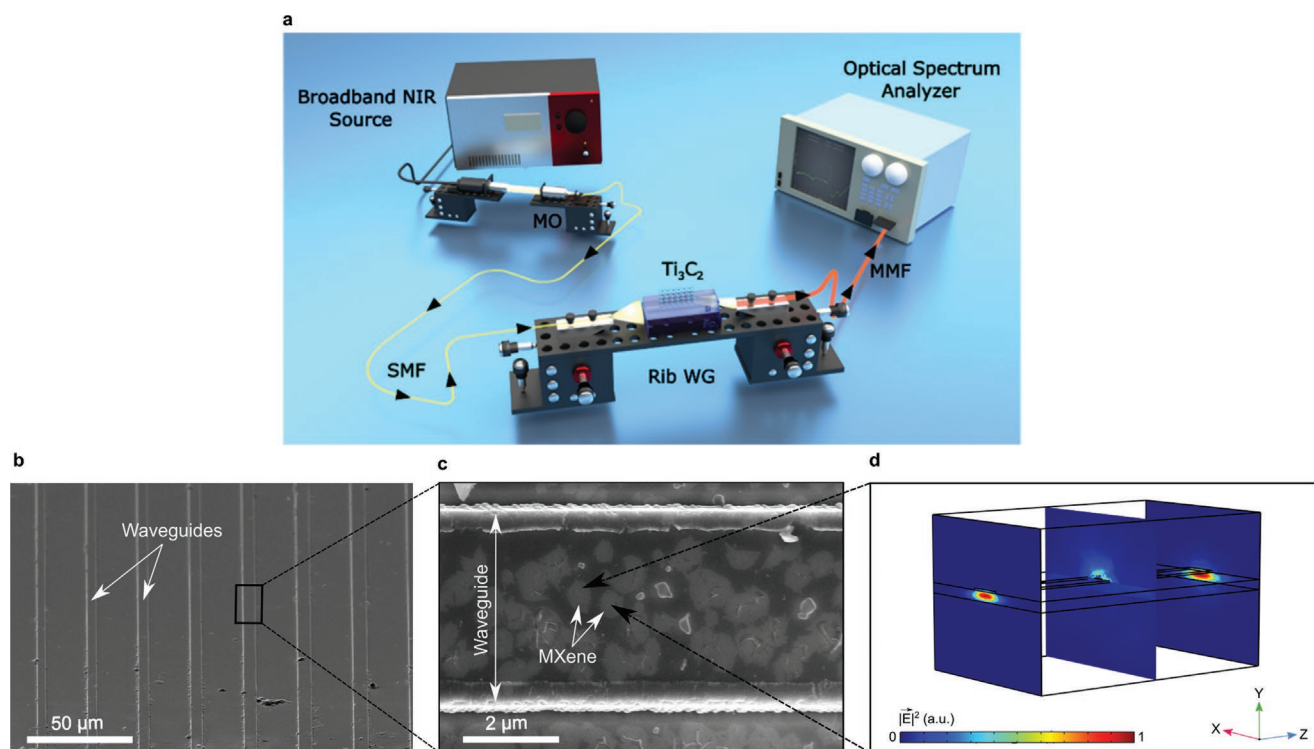


Figure 3. Experimental evidence of all-optical nonlinear activation function on a chip. a) Schematics of the experimental setup with broadband input light coupled to the waveguide (WG) and collected from the waveguide output facet via optical fiber into a spectrum analyzer (SMF - single mode fiber. MMF: multimode fiber). b,c) Top-view SEM images of blank reference waveguides (b) and metasurface overlayer of MXene on a rib waveguide (c). d) Calculated field distribution of optical mode propagating in the waveguide core and interacting with MXene nanodisks indicated by arrows in subplot with the dispersion of MXene (in the Supporting Information).

Figure 3b shows a scanning electron microscopy (SEM) image of the top view on reference waveguides, while Figure 3c shows an SEM image of the top view on waveguides covered by a MXene-flake-based metasurface overlayer. To better understand the light-matter interaction, specifically the interaction between the evanescent waves and MXenes overlayer, we numerically explored a unit cell effect made of two MXene nanodisks atop the silicon, illuminated by the evanescent-wave-studied rib waveguide. Calculated results show the extinction cross-section curve as in Figure S3a (Supporting Information) with two peaks. The smaller peak appears at a shorter wavelength (around 1020 nm), while the larger peak appears at a longer wavelength (around 1560 nm). Figure S3b (Supporting Information) shows the power loss density in a slice through the MXene nanodisks to assess the intensity dependence in the proposed hybrid system. The numerical evidence of the MXene-light interactions can be achieved via modeling unpolarized optical electromagnetic (EM) waves incident upon the input facet of the Si rib waveguide covered with MXene material, as shown in Figure 3d. The interaction between the optical evanescent waves and MXene flake overlayer leads to optical losses within the material due to its absorption. It simultaneously leads to scattering light in all directions. While the optical modes travel without disturbance through the waveguide without the presence of the MXene flake overlayer, the

transmission decreases because of increased optical losses due to changes in the optical modes' waveguiding boundary condition.

The experimentally obtained transmittance as a function of the wavelength for the lowest input power (6%) is shown in Figure 4b, together with the corresponding fitting curve according to Equation (2). Considering the first eight modes supported by the waveguide $m = 0, 1, \dots, 8$, the transmittance fitting was calculated in the wavelength range from 1260 to 1600 nm. The experimental results show good correspondence with the theoretically computed values with a total relative error of 2.34%. The normalized measured transmittance (for all the signals, relative to the maximal obtained measured value) as a function of both wavelength and input power is shown in Figure 4c, highlighting the studied system's possible optical transfer functions. The silicon waveguide covered with MXene flake overlayer configuration exhibits a broad spectral optical response to the incident light power appearing in a wavelength region in telecom bands which are commonly used in optical communication devices. Each spectral window is highlighted in transparent boxes: original (O-band), extended (E-band), short wavelengths (S-band), conventional (C-band), and long wavelengths (L-band). For the MXene-waveguide configuration, quadratic fitting was used due to the nonlinear operation acting on the optical intensity, which is directly related to the electric

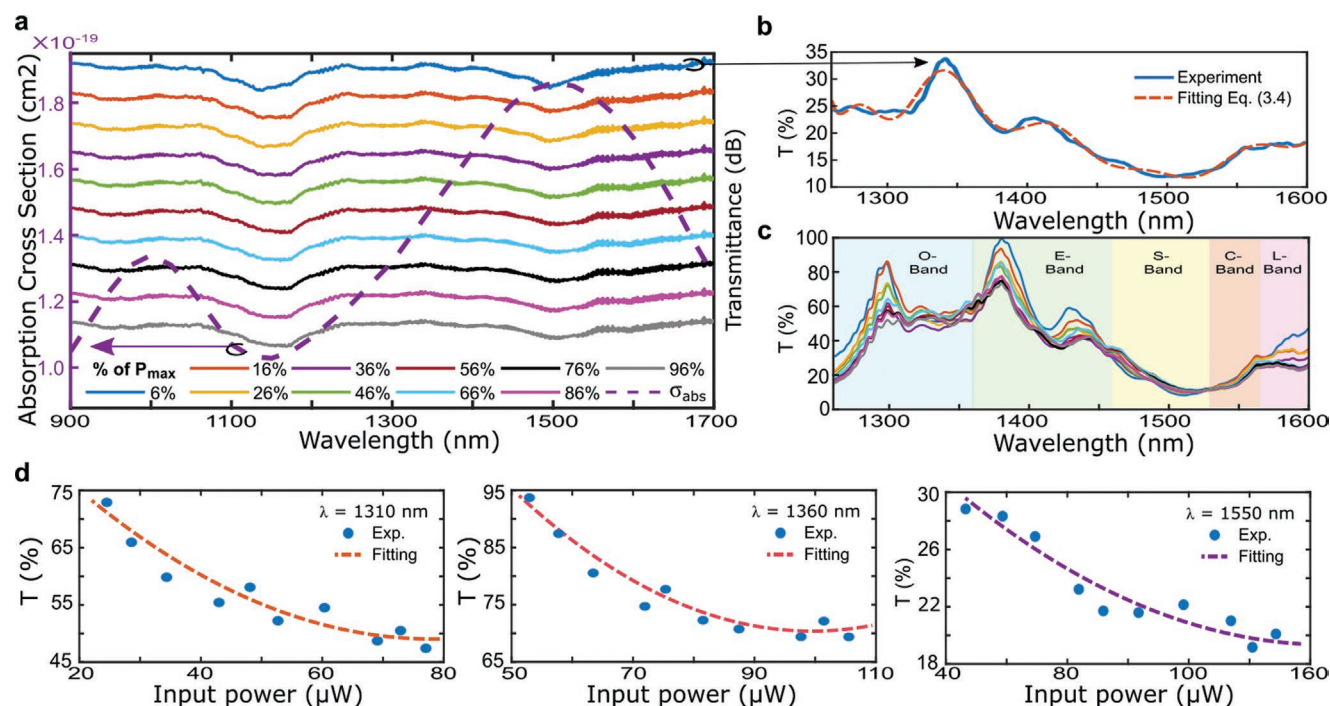


Figure 4. Experimental results of a silicon waveguide with MXene flake overlayer. a) The measured transmittance spectra from silicon rib waveguide covered with MXene flakes for different input powers varying from 6% to 96% (from top to bottom). The measurement values related to the lowest input power are shown in subplot (b), and the others are plotted with a step of -15 dB. The simulated absorption cross-section spectra $\sigma_{\text{abs}}(\lambda)$ of the MXene nanodisks atop a silicon waveguide is indicated by the purple dashed curve. b) The experimentally obtained transmittance (blue curve) as a function of the wavelength for the lowest input power (6%) and the corresponding fitting according to Equation (2) (dashed orange curve). c) Zoom-in of the normalized measured transmittance (relative to the maximum obtained measured value) dependence on the wavelength showing a broad optical response to the incident light power that appears in a wavelength region corresponding to the telecom bands (each spectral window highlighted in a transparent box). The curves' color corresponding to the same signals appears in subplot (a) legend. d) Experimentally measured nonlinear transmittance responses and the corresponding calculated fitted curves at various operating wavelengths in the "O" (left subplot, orange), "E" (middle subplot, red), and "C" (right subplot, purple) bands.

field amplitude with squaring proportionality. In other words, the incident optical field intensity associated with the photon flux is quadratically dependent on the applied optical electric field (i.e., $I = 2\epsilon_0 c |E|^2$). The experimentally measured nonlinear transmittance responses and the corresponding calculated fitted curves at various operating wavelengths are shown in Figure 4d for the O-band (1310 nm, orange curve), E-band (1360 nm red curve), and C-band (1550 nm, purple). These proposed novel configurations can serve as all-optical nonlinear units in which the achievable nonlinear transfer functions can be flexibly designed depending on the devices' operating wavelength without modifying their physical structure. In particular, they operate at commonly used optical communication wavelength bands (each spectral window is highlighted in a transparent box in Figure 4c).

2.4. MXene Saturable Absorber

A further alternative approach to realize the nonlinear activation function is utilizing the optical nonlinearity via the effect of saturable absorption, for which the absorption decreases with an increase in the input light intensity. This could be

expressed by the material absorption coefficient at a given wavelength as $\alpha = \alpha_0 / (1 + I/I_s)$, where α_0 is the linear absorption coefficient, I and I_s are the incident and saturation intensities. Recently, 2D Ti_3CNT_x was found to exhibit nonlinear saturable absorption (or increased transmittance) at higher light fluences.^[29,50] In addition, it was shown that the saturation fluence and modulation depth of Ti_3CNT_x MXene depend on the film thickness.^[29] To experimentally extract the nonlinear optical response, we fabricated four spray-coated samples of thin films of $\text{Ti}_3\text{C}_2\text{T}_x$ on BK-7 glass, with an increasing thickness between 50 and 90 nm. One may expect to observe the saturable absorption property of MXene thin film via free-space illumination measurement. For this, we used unpolarized light illuminating a 50 nm MXene film on a BK-7 substrate and collected via the focusing objective into the multimode optical fiber directly connected to the optical spectrum analyzer illustrated in Figure 5a. The measured transmission spectra of MXene thin-film response to input powers vary from 6% to 80%, as shown in Figure 5b. It shows that the saturated absorption is broadband. The calculated linear optical transmittance of the $\text{Ti}_3\text{C}_2\text{T}_x$ films on a glass substrate as a function of wavelength (Figure 5c) decreases with an increase in the film thickness, which correlates well with experimental measurements.

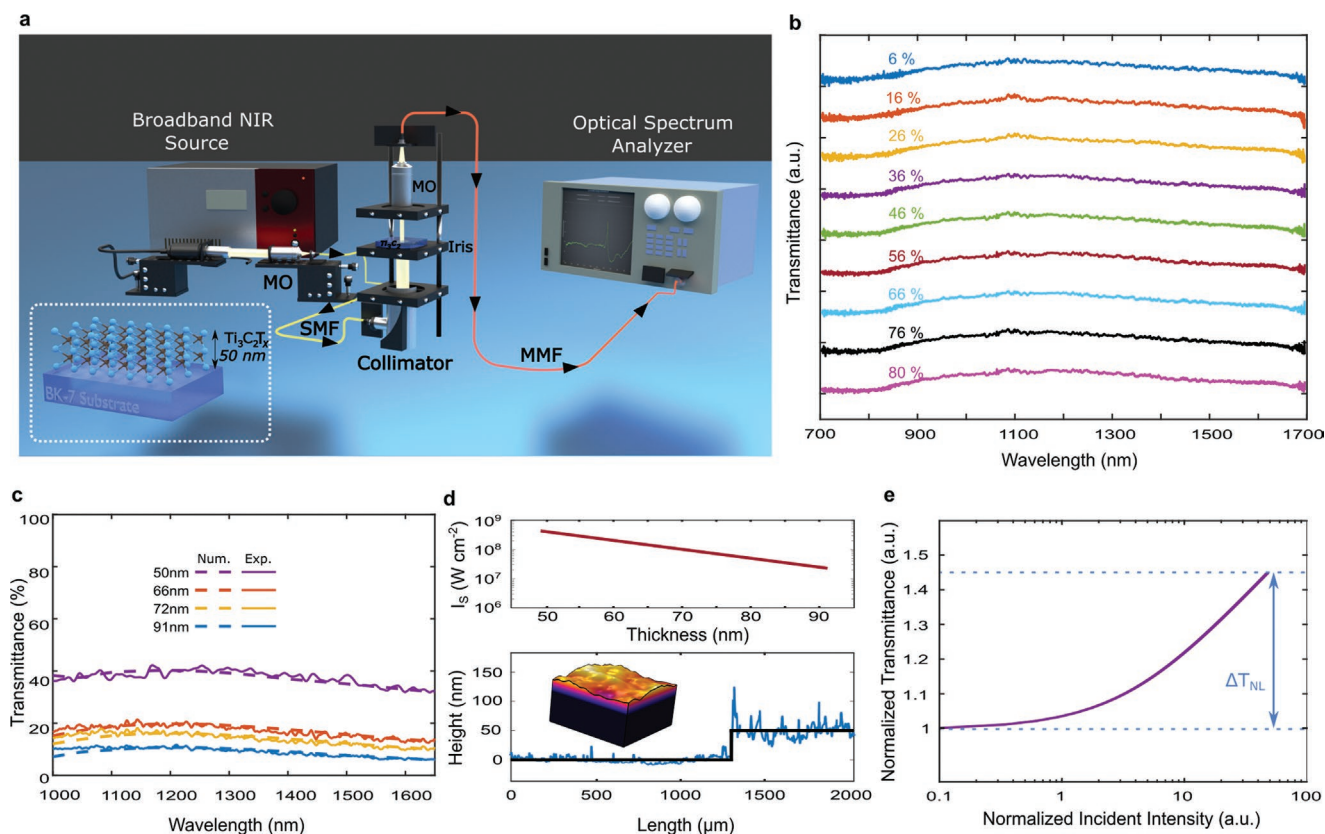


Figure 5. Free-space response of MXene thin films to input power. a) Rendered transmission setup with inset showing a thin film of $\text{Ti}_3\text{C}_2\text{T}_x$ on BK-7 glass; microscope objective (MO), single-mode fiber (SMF), multimode fiber (MMF). b) Measured transmission spectra for MXene thin films with 50 nm thickness on BK-7 substrate, for various input powers from 6% to 80% (top to bottom). c) Measured (solid) versus calculated (dashed) transmission spectra for MXene films with thicknesses (top to bottom) of 50, 67, 72, and 91 nm. d) (top) The saturation intensity versus MXene thickness at the wavelength of 1550 nm; (bottom) the measured thickness of MXene with profilometer (average marked by the black line) compared to the modeled random roughness of MXene thin film on BK-7 substrate of the depth of 8 nm. e) Nonlinear transmission of the 50 nm MXene film as a function of input intensity evaluated from the transmission waveguide spectroscopy at the wavelength of 1550 nm.

The model considers the measured refractive index and extinction coefficient for different thicknesses, with surface roughness measured by a profilometer. When the incident intensity at which the absorption coefficient is half of the linear absorption coefficient (i.e., $\alpha = \alpha_0/2$) defined as the saturation intensity, which is dependent on the film thickness (Figure 5d, top). We note that the random roughness of spin-coated films (Figure 5d, bottom) does not affect the observed nonlinear transmission effect. This is not surprising because the wavelength of the incident light is much larger (>110-fold higher) than the sample's roughness which is of several nanometers scale. The modulation depth, as depicted in Figure 5e, can be determined by the maximum change in saturable absorber for a given wavelength as follows: $\Delta T_{\text{NL}}(\lambda) = [T_{\text{NL}}(\lambda) - T_{\text{L}}(\lambda)] / T_{\text{L}}(\lambda)$, where T_{NL} and T_{L} are nonlinear and linear transmissions, respectively.

2.5. Operation of the Nonlinear Activation Function

As a first step, we experimentally achieved a set of transmission spectrum measurements for each nonlinear activation function mechanism. The transmission spectrum was monitored on an optical spectrum analyzer to observe the nonlinear responses by controlling the input optical power. Each set consists of several measurements for various input powers from 6% to 96%. Proceeding further, we obtain transfer functions representing the instantaneous input and output power amplitudes measured at a specific wavelength (detailed in the Experimental Section). The wavelength dependence of optical responses allows us to tune the nonlinear activation function shape. These transfer functions represent the device's nonlinear optical responses by output power versus input power relation. We note that these observed nonlinear functions represent a subset of functions achievable by our devices without modifying the structure of the devices. A generic activation function squashes a real input number to a fixed interval specified with unitless (Figure S4, Supporting Information). By contrast, realistic optical activation function input and output units are in the context of spectral quantities specified with units of mW nm^{-1} . Thus, in this hardware–software coinvestigation, they are regarded as the relation of power in and power out. Here, we aim to validate the performance of well-known DNN architectures by focusing on the nonlinear operation shape formed by the studied photonics devices by examining their functionality in a conventional machine-learning task. Therefore, the model avoids noises generated by the device or those induced by the OIU (through the summation of the weighted input signals), which could, in a future investigation, be scaled for large-scale NN deployment.

2.6. All-Optical Neural Network Emulation

Next, we introduced the obtained by us nonlinear optical responses as neurons' nonlinear activation function in a conventional machine-learning task: a handwritten digit image to be classified. Figure 6a shows the studied structure of feed-forward DNN comprising two hidden layers, each comprising 100 neurons, and resulting in outputs in the range from 0 to

9. Thus, the output layer in our network has only ten neurons belonging to one of ten categories, representing digits from 0 to 9. We aim to identify the representing numbers for each input image using DNN, as shown in Figure 6a; several outputs predicted labels correspond to four input handwritten digit images. Feeding each image to the input layer requires preprocessing each 2D matrix of a handwritten digit image to a high-dimensional vector. Then, the input signals can be encoded in the amplitude of optical pulses when propagating through the photonic integrated circuit. Each layer of the DNN comprises optical interference and nonlinearity units, which implement optical matrix multiplication and nonlinear operation, respectively. As discussed earlier, the input optical signals are weighted and combined through a mesh of integrated Mach–Zehnder interferometers. However, employing a MXene metasurface overlayer on waveguide or MXene thin-film configurations can achieve the nonlinear activation function. In addition, we noted that between two consecutive layers, on each output connection, the nonlinear activation function is placed (e.g., each neuron sums all the weighted inputs from neurons in the preceding layer and then applies the nonlinear activation function).

One can effectively evaluate their functionality by emulating the behavior of the experimentally implementing nonlinear optical operations of the studied approaches as neurons' nonlinear activation function in photonic DNN. To this end, we utilized the deep-learning framework in the Matlab environment, to emulate the photonic DNN's performance in terms of accuracy and loss compared to those obtained with software-based nonlinear activation functions for the MNIST dataset. In particular, we trained our networks with two sets of nonlinear activation functions: the proposed all-optical devices and software-based commonly used in machine-learning applications. These transform functions are obtained from experimentally measurements at various operating wavelengths for MXene metasurface overlayer on waveguide and MXene thin-film configurations, representing power in to power out relation, as shown in Figure 6b. By contrast, Figure S4 (Supporting Information) shows the commonly used software-based nonlinear activation function we employed to compare our photonic configurations—the Rectified Linear Unit, Softplus, Exponential Linear Unit, and Mish. To achieve the mathematical model of the nonlinear operations used in photonic neural network emulation, we considered a f_{NL} that models the transfer functions associated with each studied mechanism due to MXene–light interaction (details presented in the Experimental Section).

During the training and testing processes, we considered three separate datasets. While the training dataset was randomly broken down into two subsets, 80% and 20% (e.g., 48 000 and 12 000 images, respectively), to train and validate the model. The testing dataset ensures the model can classify the images without acknowledging the data beforehand, based on learning about the data features. It is worth mentioning, that through the validation process, the weights in the model are not updated based on the loss calculated. Figure 6c shows the network prediction accuracy when the network is trained for 50 epochs, indicating that all the proposed all-optical nonlinear activation functions achieve competitive classification

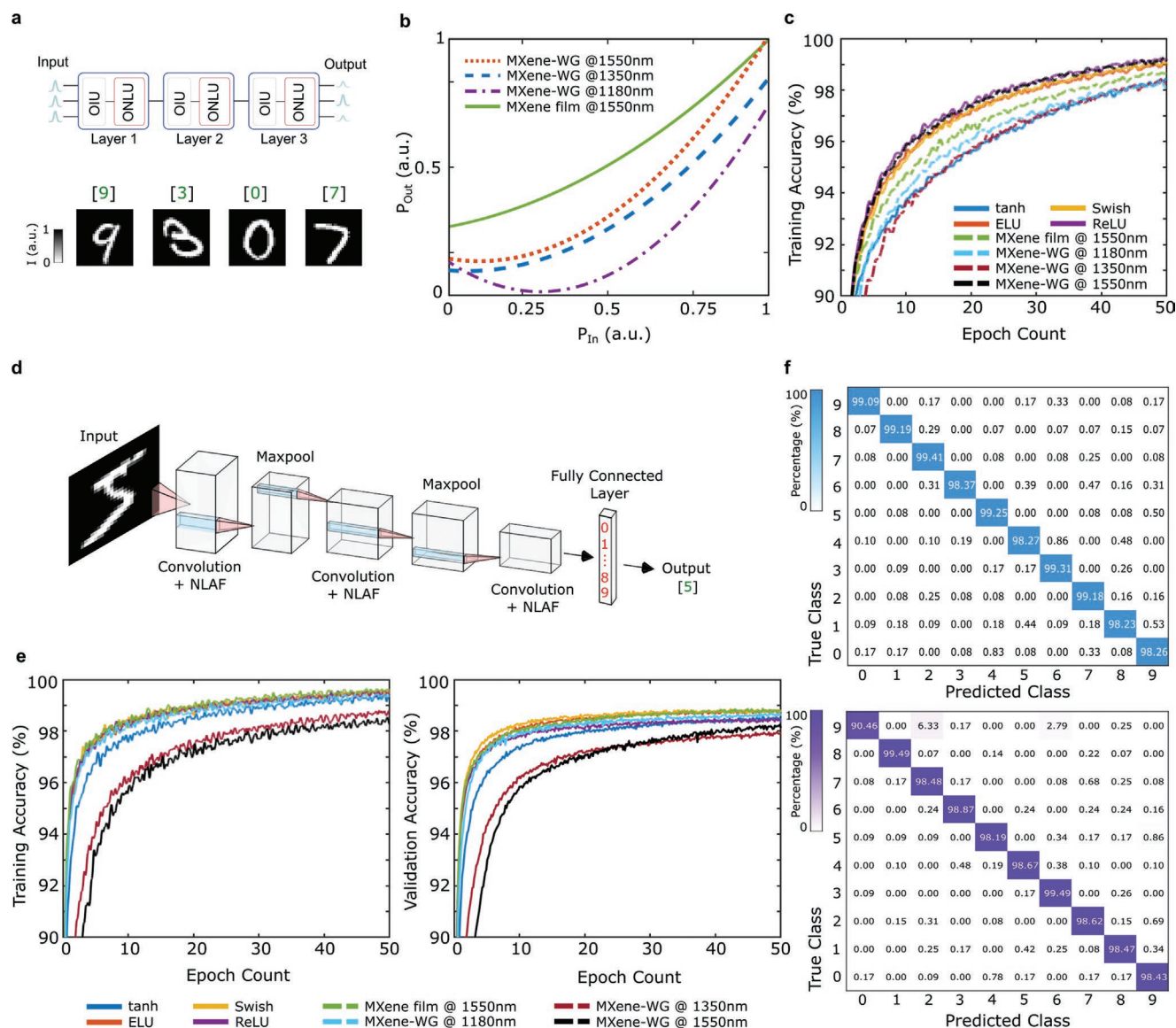


Figure 6. A high degree of precision MNIST classification with MXene nonlinear activation function. a) Schematics of the emulated three-layer structure fully connected network. Each layer of the DNN is composed of optical interference and nonlinearity units. (bottom) Several predicted labels correspond to four input handwritten digit images. b) Different MXene-based activation functions represent the “power in” to “power out” relation for various operating wavelengths. c) Network prediction accuracy as a function of epoch count during the training process, with proposed all-optical nonlinear activation functions considering MXene metasurface overlayer on waveguide and MXene thin film compared to standard software-based nonlinear activation functions. d) Schematic illustration of decomposing the studied convolutional neural network into unique layers with all-optical nonlinear activation function operations. The input is a handwritten digit image resulting in outputs in the range of 0–9. e) Model accuracy comparison between the proposed all-optical MXene-based and software-based nonlinear activation functions during the training and validation processes. f) Experimental confusion matrices of the MNIST classification, using the transfer functions of MXene thin film (blue) and MXene metasurface overlayer on waveguide (purple) at a wavelength of 1550 nm. The model achieved 98.9% and 97.4% recognition accuracy of the test dataset, respectively.

accuracies against the standard software-based nonlinear activation functions on the MNIST dataset. The validation data accuracy and loss verify the training dataset (Figure S5, Supporting Information). All the proposed photonic nonlinear operations considering MXene metasurface overlayer on waveguide and MXene thin film achieve accuracies between 97.9% and 99.1%.

To better understand the functionality of the proposed nonlinear operation mechanisms compared to the well-established and commonly used nonlinear activation functions, we

emulated their behavior in different network architectures, utilizing a convolutional NN (CNN). The task of the CNN is the same, requiring it to identify the representing numbers for each input image of the MNIST handwritten digit dataset. This class of networks operates under a different approach as compared to the first studied network. As depicted in Figure 6d, the studied CNN is decomposed into unique layers. The input is a handwritten digit image processed by convolutions, pooling, operation of the proposed all-optical nonlinear activation

function, a fully connected layer followed by a softmax activation, and the output resulting in the range of 0–9. Figure 6e represents an accurate comparison between the proposed all-optical MXene-based and software-based nonlinear activation functions during the training and validation processes. Also, in this case of CNN, one can see that the proposed activation mechanisms provide competitive performance in terms of accuracy and loss as a function of epoch with respect to the well-established and commonly used nonlinear activation functions. After training and validating the networks, they predicted the output of unlabeled data in the testing dataset. With deep structured learning architectures based on only linear operation, NN is limited in its performance and can only deal with simple problems. The nonlinear activation function (AF) is the essence of the NN's powerful expression ability to compute nontrivial problems using a small number of nodes. The most important feature of an activation function is its ability to add nonlinearity into the learning of the neurons' network. Namely, it influences the network's speed (in terms of data and epochs it needs) and the accuracy of the task it performs. Thus, an OIU alone is insufficient for a photonic device to act as a building block in deep structured learning applications, and some optical nonlinearities must be introduced in the system. It needs to be emphasized that there is no one best AF for all the NN architectures' computing tasks. Individual AF may be better in some cases but may be worse in others. Therefore, different optical AF (i.e., shape) implementations are required due to the different computing tasks. For instance, for feed forward neural network (FFNN), MXene-WG@1550 nm is preferred, but for CNN, MXene-WG@1550 nm demonstrates lower performance and, in this case, MXene film@1550 nm is preferred, therefore in Figure 6c, MXene-WG@1550 nm shows the best training accuracy, whereas, in Figure 6e, it showed the lowest training accuracy.

Figure 6f shows the experimental confusion matrices of the MNIST classification, using the transfer functions of MXene thin film (blue) and MXene metasurface overlayer on waveguide (purple) at an operating wavelength of 1550 nm, achieving 98.9% and 97.4% recognition accuracy of the test dataset, respectively. Moreover, besides this classification example, there are other applications where such nonlinear activation functions are routinely used for artificial neural network tasks and in a wide variety of types of networks, in addition to the two examples shown here.

Taking into account the availability of dozens of stoichiometric and solid-solution MXenes with a wide range of optical properties and plasmon resonances covering the wavelength from UV to IR, there is an attractive perspective for designing photonic devices with MXenes beyond $\text{Ti}_3\text{C}_2\text{T}_x$.

3. Conclusion

We have demonstrated an all-optical nonlinear activation function with MXene flakes operating in a wide spectral range. We fabricated $\text{Ti}_3\text{C}_2\text{T}_x$ MXene thin films and MXene overlayers on waveguides. Here the reconfigurable material platform is proposed, so the all-optical nonlinear transform functions via the MXene-based devices' optical responses are achieved in the

cases of 1) evanescent excitation on a chip, and 2) in free-space configurations. Proposed here MXene-based configuration exhibits broadband optical responses in contrast to ref. [51]. In terms of technology readiness level: our devices are ready to be used and do not require additional components such as wavelength modulators or diabatic mode converters with advanced mode matching, for integrating with existing and developed optical NN architectures. Other AF architectures made of different conventional materials, usually have operating wavelengths as the transition wavelength of atoms, and the working bandwidth is limited. However, the wavelength and bandwidth may not be compatible with the telecom windows and other guided-wave optics building block materials operating at the conventional band (C-band) to take advantage of the lower loss commonly used for optical communication in the silicon platform. Hence, to integrate such AFs into photonic deep-structured learning architectures, other essential components need to be considered: an interface based on light frequency conversion that can convert the light's wavelength from the optical OIU (telecommunications wavelengths) to the operating wavelength of the AFs. Although nonlinear activation functions were suggested and measured for use in optical neural networks, they were never implemented with MXene family materials which consist of a wide range of optical properties and plasmon resonances covering the wavelengths from UV to IR for designing photonic devices with MXenes beyond also $\text{Ti}_3\text{C}_2\text{T}_x$ that we used in our study. We note that the response time in our all-optical system is the speed of light in matter, namely c/n with n of silicon at 1550 nm is 3.48. The connectivity to other neurons can be implemented via the output of our device and can induce the next neuron in the network. We numerically explored a unit cell effect made of two MXene nanodisks atop the silicon waveguide. The resulting transmission spectrum dips can be explained as localized surface plasmon excitation at wavelengths of 1020 and 1560 nm. In principle, the MXene flakes form stable colloidal solutions in water without additives and surfactants due to their negative surface charge. Therefore, they can be deposited from pure water solution or other polar solvents, such as alcohols. This property is an important advantage of MXenes over graphene, carbon nanotubes (CNTs), metal nanoparticles, etc. The stochastic process here is statistically determined through: 1) the constant concentration of MXene in water and 2) the dripped position being perpendicular to the waveguide surface. For large-scale photonics-based DNN deployment, both mass concentration and a polar solvent can provide a tuning of the randomness. Therefore, it is possible to achieve a tailor-made nonlinearity response by controlling the extinction properties of the MXene metasurface. Our emulator showed compatible performance of the proposed activation mechanisms based on a MXene metasurface overlayer on the waveguide and a MXene thin film, in terms of accuracy and loss as a function of epoch with respect to the well-established and commonly used nonlinear activation functions in machine-learning tasks. The nonlinear response of the activation function was achieved due to the saturable absorber property of MXene. The all-optically implemented activation function demonstrated in this work may open a new chapter in the development of advanced materials for broadband deep-structured learning operation and for efficient computation.

4. Experimental Section

MXene Thin-Film Preparation: $\text{Ti}_3\text{C}_2\text{T}_x$ was synthesized by the selective etching of Ti_3AlC_2 MAX phase powder (325 mesh) with a mixture of HF (48.5–51%, Acros Organics) and HCl (36.5–38%, Fisher Chemical) acids.^[52] Typically, 2 mL of HF, 12 mL of HCl, and 6 mL of deionized (DI) water were mixed. After that, 1 g of MAX phase powder was added to the solution and stirred for 24 h at 35 °C. After etching, the reaction product was washed with DI water using the centrifuge at 3500 rpm for 2 min until pH >6. The obtained sediment was dispersed in a 0.5 M LiCl solution. The mixture was shaken for 15 min and then centrifuged at 3500 rpm for 10 min several times until the sediment was delaminated and swelled. The swelled sediment was dispersed in DI water and then centrifuged at 3500 rpm for 10 min. After that, the dark supernatant containing primarily single-layer MXene sheets was collected for spray-coating. Finally, four thin films of ≈50–90 nm thicknesses $\text{Ti}_3\text{C}_2\text{T}_x$ were spray-coated on a borosilicate glass (BK-7) substrate with a ratio of 4.5 mg mL⁻¹ DI water.

MXene Thin-Film Characterization: To characterize the surface roughness and thickness of the fabricated MXene films, topography measurements were performed with the Stylus profilometer, Veeco Dektak-8.

Ellipsometric Spectrometry: The optical parameters of MXene, namely, the refractive index n and extinction coefficient k were obtained via a spectroscopic ellipsometer. Spectroscopic ellipsometer measurements were performed in the wavelength range of 245–1690 nm. The samples consisted of a BK-7 glass substrate with $\text{Ti}_3\text{C}_2\text{T}_x$ coating of thicknesses of ≈50, 67, 72, and 91 nm.

Waveguide Fabrication: The rib waveguides were fabricated as detailed in ref. [53] based on a silicon-on-insulator wafer with a silicon carrier, 2 μm of silica SiO_2 and 2 μm of silicon. E-beam resist poly(methyl methacrylate) (PMMA) 950k was used together with a line pattern mask via a conventional photolithography process. Once the PMMA resist was developed, aluminum was evaporated to serve as a hard mask with a thickness of 250 nm via an electron gun evaporator. Next, the chip was soaked in acetone for 4 h (liftoff process) and the chip was cleaned with isopropanol. Eventually, the chip was dry-etched with SF_6 + Ar and O_2 to achieve straight lines and 90° waveguide walls. The residue of the Al hard mask was removed with a 400K developer.

Procedure for Preparing MXene Flakes for Waveguide Overlayer: The concept of waveguide overlayer is schematically shown in Figure 2a and the preparation procedure in Figure 2b. As a monolayer, the MXene might be oxidized. The assembly of a colloidal solution could prevent the oxidation arising from the environment. In addition, no significant changes in the nonlinearity of the optical response were expected in the presence of a protective cladding, taking into account the $\text{Ti}_3\text{C}_2\text{T}_x$ surface terminations such as –O, –OH, and –F. It is worth mentioning that several nanometers of transparent dielectric protective cladding would not affect the performance of the device. The Ti_3AlC_2 powders were synthesized by mixing titanium carbide (Alfa Aesar, 99.5% 2 μm), aluminum (Alfa Aesar, 99.5%, 325 mesh), and titanium (Alfa Aesar, 99.5%, 325 mesh) powders in a molar ratio of 2:1:1, respectively. The powders were mixed in a horizontal rotary mixer at 100 rpm for 24 h and then heated under Ar flow at 1400 °C for 3 h. The heating and cooling rates were set at 5 °C min⁻¹. The resulting loosely sintered block was ball-milled to powders and passed through a 400 mesh (<38 μm) sieve. The Ti_3AlC_2 powder was etched in a LiF and HCl solution. Initially, 1 g of LiF (Alfa Aesar, 99.5%, 325 mesh) was dissolved in 10 mL of 12 M HCl (Fisher Scientific). Later, 1 g of the Ti_3AlC_2 powder was slowly added to the solution and stirred for 24 h at 35 °C and 300 rpm. After etching, the slurry was transferred into a 50 mL centrifuge tube and DI water was added to fill the remaining volume. It was then centrifuged at 2300 rcf for 2 min and the resulting clear supernatant was discarded. The same washing process was repeated several times until the pH of the solution was ≈7, at which point DI water was added to the resulting $\text{Ti}_3\text{C}_2\text{T}_x$ “clay” and the mixture was sonicated under bubbling Ar flow for 1 h. To avoid oxidation, the bath temperature was kept below 20 °C using ice. The solution was then centrifuged for 1 h at 4700 rcf and the supernatant

was pipetted off, dried in a drying oven at 120 °C for 12 h, and sealed under Ar for storage and future use. To obtain the MXene flake solution, 0.1 g of dry $\text{Ti}_3\text{C}_2\text{T}_x$ was added to 10 mL DI water and sonicated in an ultrasonic bath for 5 min, resulting in a solution of dispersed $\text{Ti}_3\text{C}_2\text{T}_x$ suspension with a concentration of 0.01 g mL⁻¹.

Scanning Electron Microscopy: The surface SEM images of blank reference waveguides and metasurface overlayer of MXene on a rib waveguide were examined using a high-resolution scanning electron microscope (FEI Verios 460L).

Numerical Simulation: The absorption and extinction cross-section profiles of the nanodisks atop the waveguide were calculated numerically. The 3D simulation was carried out using a commercial COMSOL Multiphysics 5.6 software based on the finite element analysis method in wave optics module, as a unit cell with periodic boundary conditions. Mesh was explored to ensure the accuracy of the calculated results. The dielectric constant of the material entirely defined the material optical properties. Therefore, the empirical dielectric functions of the silicon and silica were taken from the Refractive-index database (<https://refractiveindex.info>). By contrast, the dielectric function of MXene (Figure S4, Supporting Information) was obtained via the measured refractive index distribution with a spectroscopic ellipsometer. In the simulation, the thickness of the MXene nanodisks was set to 10 nm with a radius of 0.25 μm, as evaluated from SEM images of the fabricated MXene flakes.

Experimental Systems for Nonlinear Transmission Measurements: Two experimental systems were used to measure the nonlinearity in the optical response of the two MXene configurations. Both setups were used for achieving a broadband spectrum of the transmitted light through the proposed configurations using standard optical communication components. All setups were constructed in a clean room environment. The energy source for optical computing was generated using a supercontinuum white-light laser source (SuperK EXTREME EXW-12, NKT Photonics), bandwidth from 390 to 2400 nm, fiber delivered and collimated with an output power of 5.5 W. The beam was focused on single-mode fiber (P1-1550A-FC, 1460–1620 nm, Ø125 μm cladding, Thorlabs) using a 10× infinity-corrected imaging microscope objective (RMS10X, with a numerical aperture of 0.25, Olympus).

For silicon WG covered with MXene flake configuration, inline measurements setup was used with butt-coupled light from a single-mode fiber to the input waveguide facet. The output optical spectra were collected via the conventional silica multimode fiber (MMF 50:125 μm core to cladding, respectively) directly into the optical spectrum analyzer (AQ6370D, Yokogawa), as shown in Figure 3a. The fibers were held with 3-axis piezoelectric stages that allowed flexibility for precise adjustment of the fibers to the waveguide input and output facets. In addition, the waveguide was imaged (top view) onto the camera (Axiocam, ZEISS) using a microscope (Stemi SV 6, ZEISS) for accurate inspection, characterization, and alignment. Prior to the measurements, the MXene flake solution was prepared with a ratio of 1 mg per 100 mL DI water. Then, a droplet of 2 μL of the solution was dripped atop the nanophotonic rib waveguide using a micropipette and dried up in the cleanroom environment.

MXene thin-film characterization was performed with the transmission setup we built, shown in Figure 5a. The coherent supercontinuum generation light with constant pump power at the set level was collimated via a protected silver reflective collimator (RC04FC-P01, 450 nm–20 μm, Ø4 mm beam, Thorlabs), then passed through an iris. The sample was mounted on a fixed stage and illuminated by the unpolarized supercontinuum generation white light, with a spot size of 100 μm onto the MXene nanofilm on a BK-7 glass substrate. The transmitted light was collected into the optical spectrum analyzer via MMF using a 4× infinity-corrected imaging microscope objective (RMS4X, with a numerical aperture of 0.1, Olympus). The laser was operated in modulated power mode that generated picosecond pulses with a repetition rate of 78.56 MHz.

Spectrometry Measurements: To observe the optical responses due to MXene–light interaction, the intensity of the transmitted light when the MXene was present was first measured. As a reference measurement,

the spectra without the contribution of MXene were collected. The differential transmission spectra were then plotted (Figures 4a and 5b), which were given by

$$\Delta T(\lambda) = \frac{|T_{\text{MXene}}(\lambda)|^2}{|T_{\text{Ref}}(\lambda)|^2} \quad (1)$$

In the case of MXene flakes overlayer on a waveguide, $|T_{\text{MXene}}|^2$ was the transmittance when an unpolarized light was coupled to a rib waveguide with the presence of $\text{Ti}_3\text{C}_2\text{X}$ on the top surface, whereas $|T_{\text{Ref}}|^2$ was the transmittance spectra collected from a blank reference waveguide. In the case of MXene thin films $|T_{\text{MXene}}|^2$ was the transmittance when the unpolarized light hit the BK-7 substrate, which was covered with $\text{Ti}_3\text{C}_2\text{X}$ nanofilm, whereas $|T_{\text{Ref}}|^2$ was the transmittance through the glass medium. In each case, ten measurements were carried out to follow the changes in input power.

Activation Function Settings: To obtain a mathematical function that modeled the transfer function of the all-optical activation function to be used in photonic neural network emulation, data points were fitted from the experimental results to the total broadband optical transmittance of the devices.

For the MXene–waveguide configuration, quadratic curves were fitted due to the nonlinear operation acting on the optical intensity, which was directly related to the electric field amplitude with squaring proportionality. The total transmittance was defined fundamentally by the power losses within the interaction length of the MXene–waveguide. Therefore, the transmittance through the MXene flakes overlayer on a waveguide system was obtained as in ref. [54]

$$T(\lambda) = \left| \sum_{\gamma=1, j, m} C_{\gamma j} \exp(-i\alpha_{\gamma j} L) \right|^2 \quad (2)$$

where $C_{\gamma j} = (I_{j0, \gamma} + I_{j1, \gamma})^2 / (4I_{j0, \gamma} I_{j1, \gamma})$, L is the interaction length, $\alpha_{\gamma j}$ is an attenuation coefficient of modes in a region covered with MXene flakes, j are the guided modes influenced by the MXene, and $j0$ are the guided modes in a pure dielectric waveguide.

For the MXene thin-film configuration, the saturable absorption property of MXene was utilized. A saturable absorber material was characterized by the dependence of its absorption on the incident laser intensity. Therefore, at a given wavelength λ , the transmission through the MXene thin film could be expressed as follows^[55]

$$T(I) = 1 - \Delta T_{\text{NL}} \exp\left(\frac{-I}{I_s}\right) - T_{\text{ns}} \quad (3)$$

where ΔT_{NL} is the modulation depth, I and I_s are the incident and saturation intensities, and T_{ns} is the initial transmittance of the absorber defined fundamentally by the nonsaturable loss in the material and depended on the design of the saturable absorber.

Photonic Neural Network Emulation: The photonic DNN was modeled with a deep-learning framework in the Matlab environment, for handwritten digit classification tasks. The MNIST handwritten digit dataset consisted of 60 000 and 10 000 images belonging to training and testing, respectively. Each image was composed of a 28×28 pixel resolution associated with one of ten categories representing numbers in the range of 0–9. The training set was splitted into two subsets of 80% (training set) and 20% (validation set) images for training and validating the model. While the weights were subsequently optimized in the training process using the backpropagation algorithm,^[56] the validation set was used to validate the network without weights updating. The photonic DNN was trained by feeding data into the input layer, then based on the loss calculated from output prediction (so-called forward propagation), optimizing weights using a backpropagation algorithm using a stochastic gradient descent method. The network model used a stochastic gradient descent optimizer with a learning rate of 0.001. After forming two network architectures, their performance was evaluated using typical nonlinear activation functions. Proceeding further, the photonic NN was emulated considering the nonlinear operation based

on their transfer functions. By emulating these proposed all-optical nonlinear operations, the effect of the all-optical nonlinear activation function on the overall functionality of the NN could be estimated. The transfer functions represented the device's nonlinear optical responses by output power to input power relationships. In general, software-based nonlinear activation functions were unitless that defined a nonlinear output to input relation. Therefore, the obtained transfer functions were considered as power out to power in relation, where the actual values in the context of spectral quantities were specified with units of mW nm^{-1} (or dBm nm^{-1}). Finally, the prediction accuracy and loss of the networks were compared employing the all-optical nonlinear activation functions to those achieved with the commonly used software-based activation functions (as shown in Figure 5 and Figures S5 and S6 in the Supporting Information). These results concluded that the proposed all-optical nonlinear operations provided comparative performance as those successfully adopted in the machine-learning community.

Supporting Information

Supporting Information is available from the Wiley Online Library or from the author.

Acknowledgements

A.K. acknowledges the support of the Israel Science foundation ISF Grant No. 2598/20 and the EU ERA-NET, Ministry of Energy, Grant No. 221-11-032. D.Z. and Y.G. work on MXene synthesis was supported by a grant from the U.S. National Science Foundation Grant No. DMR- 2041050.

Conflict of Interest

The authors declare no conflict of interest.

Data Availability Statement

The data that support the findings of this study are available from the corresponding author upon reasonable request.

Keywords

artificial intelligence, integrated photonics, MXenes, silicon photonics, titanium carbide, waveguides

Received: November 4, 2022

Revised: December 1, 2022

Published online: January 29, 2023

- [1] R. S. Hegde, *Nanoscale Adv.* **2020**, 2, 1007.
- [2] B. J. Shastri, A. N. Tait, T. Ferreira de Lima, W. H. P. Pernice, H. Bhaskaran, C. D. Wright, P. R. Prucnal, *Nat. Photonics* **2021**, 15, 102.
- [3] M. H. Tahersima, K. Kojima, T. Koike-Akino, D. Jha, B. Wang, C. Lin, K. Parsons, *Sci. Rep.* **2019**, 9, 1368.
- [4] D. Liu, Y. Tan, E. Khoram, Z. Yu, *ACS Photonics* **2018**, 5, 1365.
- [5] I. Sajedian, J. Kim, J. Rho, *Microsyst. Nanoeng.* **2019**, 5, 27.
- [6] C. Qian, B. Zheng, Y. Shen, L. Jing, E. Li, L. Shen, H. Chen, *Nat. Photonics* **2020**, 14, 383.

- [7] T. W. Hughes, I. A. D. Williamson, M. Minkov, S. Fan, *Sci. Adv.* **2019**, 5, eaay6946.
- [8] Q. Zhang, H. Yu, M. Barbiero, B. Wang, M. Gu, *Light: Sci. Appl.* **2019**, 8, 42.
- [9] T. W. Hughes, M. Minkov, Y. Shi, S. Fan, *Optica* **2018**, 5, 864.
- [10] H. Zhang, M. Gu, X. D. Jiang, J. Thompson, H. Cai, S. Paesani, R. Santagati, A. Laing, Y. Zhang, M. H. Yung, Y. Z. Shi, F. K. Muhammad, G. Q. Lo, X. S. Luo, B. Dong, D. L. Kwong, L. C. Kwek, A. Q. Liu, *Nat. Commun.* **2021**, 12, 457.
- [11] Y. Zuo, B. Li, Y. Zhao, Y. Jiang, Y.-C. Chen, P. Chen, G.-B. Jo, J. Liu, S. Du, *Optica* **2019**, 6, 1132.
- [12] R. Amin, J. K. George, S. Sun, T. Ferreira de Lima, A. N. Tait, J. B. Khurgin, M. Miscuglio, B. J. Shastri, P. R. Prucnal, T. El-Ghazawi, *APL Mater.* **2019**, 7, 081112.
- [13] I. A. D. Williamson, T. W. Hughes, M. Minkov, B. Bartlett, S. Pai, S. Fan, *IEEE J. Sel. Top. Quantum Electron.* **2019**, 26, 7700412.
- [14] T. Zhou, X. Lin, J. Wu, Y. Chen, H. Xie, Y. Li, J. Fan, H. Wu, L. Fang, Q. Dai, *Nat. Photonics* **2021**, 15, 367.
- [15] Z. Yang, W. Tan, T. Zhang, C. Chen, Z. Wang, Y. Mao, C. Ma, Q. Lin, W. Bi, F. Yu, B. Yan, J. Wang, *Adv. Opt. Mater.* **2022**, 10, 2200714.
- [16] J. Feldmann, N. Youngblood, C. D. Wright, H. Bhaskaran, W. H. P. Pernice, *Nature* **2019**, 569, 208.
- [17] M. T. Hill, E. E. E. Frietman, H. de Waardt, G. Khoe, H. J. S. Dorren, *IEEE Trans. Neural Networks* **2002**, 13, 1504.
- [18] P. D. Moerland, E. Fiesler, I. Saxena, *Appl. Opt.* **1996**, 35, 5301.
- [19] C. Huang, T. Ferreira de Lima, A. Jha, S. Abbaslou, B. J. Shastri, P. R. Prucnal, in *2019 Optical Fiber Communications Conference and Exhibition (OFC)*, IEEE, Piscataway, NJ, USA **2019**, pp. 1–3.
- [20] R. Mirek, A. Opala, P. Comaron, M. Furman, M. Król, K. Tyska, B. Seredyński, D. Ballarini, D. Sanvitto, T. C. H. Liew, *Nano Lett.* **2021**, 21, 3715.
- [21] A. Ryou, J. Whitehead, M. Zhelyeznyakov, P. Anderson, C. Keskin, M. Bajcsy, A. Majumdar, *Photonics Res.* **2021**, 9, B128.
- [22] M. Miscuglio, A. Mehrabian, Z. Hu, S. I. Azzam, J. George, A. V. Kildishev, M. Pelton, V. J. Sorger, *Opt. Mater. Express* **2018**, 8, 3851.
- [23] A. Jha, C. Huang, P. R. Prucnal, *Opt. Lett.* **2020**, 45, 4819.
- [24] T. S. Rasmussen, Y. Yu, J. Mork, *Opt. Lett.* **2020**, 45, 3844.
- [25] A. Karabchevsky, A. Katiyi, A. S. Ang, A. Hazan, *Nanophotonics* **2020**, 9, 3733.
- [26] B. Anasori, Y. G. Gogotsi, *2D Metal Carbides and Nitrides (MXenes)*, Springer, Berlin, Germany **2019**.
- [27] W. Tian, A. VahidMohammadi, M. S. Reid, Z. Wang, L. Ouyang, J. Erlandsson, T. Pettersson, L. Wågberg, M. Beidaghi, M. M. Hamed, *Adv. Mater.* **2019**, 31, 1902977.
- [28] G. Wang, D. Bennett, C. Zhang, C. Ó Coileáin, M. Liang, N. McEvoy, J. J. Wang, J. Wang, K. Wang, V. Nicolosi, *Adv. Opt. Mater.* **2020**, 8, 1902021.
- [29] Y. Dong, S. Chertopalov, K. Maleski, B. Anasori, L. Hu, S. Bhattacharya, A. M. Rao, Y. Gogotsi, V. N. Mochalin, R. Podila, *Adv. Mater.* **2018**, 30, 1705714.
- [30] K. Maleski, C. E. Shuck, A. T. Fafarman, Y. Gogotsi, *Adv. Opt. Mater.* **2021**, 9, 2001563.
- [31] K. Chaudhuri, M. Alhabeb, Z. Wang, V. M. Shalae, Y. Gogotsi, A. Boltasseva, *ACS Photonics* **2018**, 5, 1115.
- [32] Y. I. Jhon, J. Koo, B. Anasori, M. Seo, J. H. Lee, Y. Gogotsi, Y. M. Jhon, *Adv. Mater.* **2017**, 29, 1702496.
- [33] Y. Shen, N. C. Harris, S. Skirlo, M. Prabhu, T. Baehr-Jones, M. Hochberg, X. Sun, S. Zhao, H. Larochelle, D. Englund, *Nat. Photonics* **2017**, 11, 441.
- [34] J. Hu, T. Lang, Z. Hong, C. Shen, G. Shi, *J. Lightwave Technol.* **2018**, 36, 2083.
- [35] J. Carolan, C. Harrold, C. Sparrow, E. Martín-López, N. J. Russell, J. W. Silverstone, P. J. Shadbolt, N. Matsuda, M. Oguma, M. Itoh, *Science* **2015**, 349, 711.
- [36] J. Chiles, S. M. Buckley, S. W. Nam, R. P. Mirin, J. M. Shainline, *APL Photonics* **2018**, 3, 106101.
- [37] A. N. Tait, M. A. Nahmias, B. J. Shastri, P. R. Prucnal, *J. Lightwave Technol.* **2014**, 32, 4029.
- [38] A. N. Tait, A. X. Wu, T. Ferreira de Lima, E. Zhou, B. J. Shastri, M. A. Nahmias, P. R. Prucnal, *IEEE J. Sel. Top. Quantum Electron.* **2016**, 22, 312.
- [39] A. N. Tait, T. Ferreira de Lima, E. Zhou, A. X. Wu, M. A. Nahmias, B. J. Shastri, P. R. Prucnal, *Sci. Rep.* **2017**, 7, 7430.
- [40] V. Bangari, B. A. Marquez, H. Miller, A. N. Tait, M. A. Nahmias, T. Ferreira de Lima, H.-T. Peng, P. R. Prucnal, B. J. Shastri, *IEEE J. Sel. Top. Quantum Electron.* **2019**, 26, 7701213.
- [41] M. Reck, A. Zeilinger, H. J. Bernstein, P. Bertani, *Phys. Rev. Lett.* **1994**, 73, 58.
- [42] X. Lin, Y. Rivenson, N. T. Yardimci, M. Veli, Y. Luo, M. Jarrahi, A. Ozcan, *Science* **2018**, 361, 1004.
- [43] Y. Luo, D. Mengu, N. T. Yardimci, Y. Rivenson, M. Veli, M. Jarrahi, A. Ozcan, *Light: Sci. Appl.* **2019**, 8, 112.
- [44] Y. Li, R. Chen, B. Sensale-Rodriguez, W. Gao, C. Yu, *Sci. Rep.* **2021**, 11, 11013.
- [45] L. Giambaghi, L. Buffoni, T. Carletti, W. Nocentini, D. Fanelli, *Nat. Commun.* **2021**, 12, 1330.
- [46] J. Li, D. Mengu, N. T. Yardimci, Y. Luo, X. Li, M. Veli, Y. Rivenson, M. Jarrahi, A. Ozcan, *Sci. Adv.* **2021**, 7, eabd7690.
- [47] M. Ghidui, M. R. Lukatskaya, M.-Q. Zhao, Y. Gogotsi, M. W. Barsoum, *Nature* **2014**, 516, 78.
- [48] E. Satheeshkumar, T. Makaryan, A. Melikyan, H. Minassian, Y. Gogotsi, M. Yoshimura, *Sci. Rep.* **2016**, 6, 32049.
- [49] T. Hu, J. Wang, H. Zhang, Z. Li, M. Hu, X. Wang, *Phys. Chem. Chem. Phys.* **2015**, 17, 9997.
- [50] Q. Wu, X. Jin, S. Chen, X. Jiang, Y. Hu, Q. Jiang, L. Wu, J. Li, Z. Zheng, M. Zhang, *Opt. Express* **2019**, 27, 10159.
- [51] G. H. Y. Li, R. Sekine, R. Nehra, R. M. Gray, L. Ledezma, Q. Guo, A. Marandi, *Nanophotonics* **2022**, <https://doi.org/10.1515/nanoph-2022-0137>.
- [52] M. Anayee, N. Kurra, M. Alhabeb, M. Seredych, M. N. Hedhili, A.-H. Emwas, H. N. Alshareef, B. Anasori, Y. Gogotsi, *Chem. Commun.* **2020**, 56, 6090.
- [53] A. Katiyi, A. Karabchevsky, *ACS Sens.* **2018**, 3, 618.
- [54] A. Karabchevsky, J. S. Wilkinson, M. N. Zervas, *Opt. Express* **2015**, 23, 14407.
- [55] S. Yamashita, *APL Photonics* **2019**, 4, 034301.
- [56] I. Goodfellow, Y. Bengio, A. Courville, *Deep Learning*, MIT Press, Cambridge, MA, USA **2016**.